CARBON 62 (2013) 393–404

Available at www.sciencedirect.com

SciVerse ScienceDirect

journal homepage: www.elsevier.com/locate/carbon

Robust growth of herringbone carbon nanofibers on layered double hydroxide derived catalysts and their applications as anodes for Li-ion batteries

Xin-Bing Cheng [a], Gui-Li Tian [a], Xiao-Fei Liu [a,b], Jing-Qi Nie [a], Meng-Qiang Zhao [a], Jia-Qi Huang [a], Wancheng Zhu [b], Ling Hu [a], Qiang Zhang [a,*], Fei Wei [a]

[a] Beijing Key Laboratory of Green Chemical Reaction Engineering and Technology, Department of Chemical Engineering, Tsinghua University, Beijing 100084, China

[b] Department of Chemical Engineering, Qufu Normal University, Shandong 273165, China

ARTICLE INFO

Article history:
Received 14 April 2013
Accepted 12 June 2013
Available online 20 June 2013

ABSTRACT

Herringbone carbon nanofibers (CNFs) were efficiently produced by chemical vapor deposition on Ni nanoparticles derived from layered double hydroxide (LDH) precursors. The as-obtained CNFs with a diameter ranging from 40 to 60 nm demonstrated herringbone morphologies when they grew on Ni/Al LDH derived catalysts both in the fixed-bed and fluidized-bed reactor. The Ni/Mg/Al, Ni/Cu/Al, as well as Ni/Mo/Mg/Al catalysts were also effective to grow herringbone CNFs. The diameter and specific surface area of the as-obtained CNFs highly depended on the catalyst composition and the growth temperature. When CNFs were grown at 550 °C on Ni/Al catalyst, the as-obtained products had an outer diameter of *ca.* 50 nm and a specific surface area of 242 $m^2 g^{-1}$, possessed a discharge capacity of 330 mAh g^{-1} as the electrode in a two-electrode coin-type cell. With the increase of the surface area, the discharge capacity increased at a rate of 0.90 mAh cm^{-2}, while the initial coulombic efficiency decreased gradually on nanocarbon anodes. This is attributed to the fact that CNFs with higher surface area afford smaller sp^2 carbon layer that facilitated more Li ions to extract from the anodes.

1. Introduction

Well arrangement of sp^2 carbon layers leads to one-dimensional (1D) carbon nanotubes (CNTs) or nanofibers, two-dimensional (2D) graphene nanosheets and three-dimensional (3D) nanostructured carbon with unexpected properties for unique applications [1,2]. For instance, CNTs and graphene are with excellent electronic, thermal, optical, and mechanical properties, which renders their promising high-end applications in the area of energy storage, heterogeneous catalysis, composites, as well as electronic devices [1,2]. The key issue for the successful applications of nanocarbon lies in the ability to pack the sp^2 carbon layers into the required nanostructures. When the sp^2 carbon sheets are packed into 1D nanocarbons, platelet carbon nanofibers (CNFs) [3–5], herringbone CNFs [6–9], and cylinder CNTs [1,2] are available. The synthesis, properties, and applications of CNTs have been widely explored during the past two decades. Up to now, CNTs have been mass produced by fluidized bed chemical vapor deposition (CVD) [10] and thermal CVD [2]. The CNT conductive slurry products are available in market to improve the performance of Li ion battery [11]. The herringbone CNFs are also a kind of promising nanocarbons [12] for the battery

* *Corresponding author:* Fax: +86 10 6277 2051.
E-mail address: zhang-qiang@mails.tsinghua.edu.cn (Q. Zhang).
0008-6223/$ - see front matter
http://dx.doi.org/10.1016/j.carbon.2013.06.023

applications for the reason that the cavities, open tips, and graphite platelets of the CNFs offer many exposed edges to provide more extra space for Li ion storage and diffusion in a Li-ion cell with high reversible capacity, high-rate performance, and good cycling stability. For instance, Fan et al. have fabricated 1D CNFs on 2D graphene sheets illustrating high reversible capacity (667 mAh/g), high rate performance, and cycling stability, which is superior to those of pure graphene, natural graphite, and CNTs [13]. The CNFs with a polygonal cross section afforded a first coulombic efficiency of 63.1% and a reversible capacity of 198.4 mAh/g at a current density of 3.7 A/g. After carbon coating, the first coulombic efficiency increased to 78.4%, and the reversible capacity was still around 197.4 mAh/g [7]. Besides, compared with the π electron orbitals exposed by CNTs, CNFs provide more edges, defects or strained regions as active sites for heteroatom functionalization and heterogeneous catalysis [14]. When the edges of CNFs were attached with ultrafine metal nanoparticles, the as-obtained CNF composites demonstrated emerging reactivity for energy conversion and storage [8,9].

Generally, CNFs are usually synthesized on metallic nanoparticle (NP) catalysts by catalytic CVD. The Fe, Co, Ni NPs distributed on supports have been employed to grow CNFs. The metal catalysts as well as the growth parameters are decisive to obtain CNFs with expected structures. However, the formation of metal NPs on supported catalysts is quite complex due to the heterogeneous nature of co-precipitation/impregnation catalysts. The use of a homogeneous catalyst precursor is quite attractive for controllable formation of metal catalyst and subsequent nanocarbon deposition. Among various catalysts, layered double hydroxides (LDHs) are considered as promising candidates for catalytic growth of 1D nanocarbons for the reason that the composition of LDHs can be anticipated and the metal can be dispersed in the framework of LDHs at an atomic scale. Simple calcination and reduction of LDHs give rise to their corresponding metal oxides or metal NPs with excellent dispersion, which have been employed as extraordinary catalysts for the growth of low dimensional nanocarbons [15,16]. Meanwhile, the physicochemical properties of such metal oxides or metal NPs (such as size, surface reactivity, composition, and the metal-support interaction) have been well tuned through controlling the calcination and reduction processes of LDHs and the selection of metal cation combination [17,18]. Therefore, ultrafine metal catalysts are available for single-/double-/few-walled CNT [19] and carbon nanoring [20] formation, while large metal catalysts derived from the LDH precursors are also effective for controllable growth of large diameter CNTs and CNFs [21,22].

In this contribution, herringbone CNFs were robustly grown on the catalysts derived from Ni based LDHs by catalytic CVD. The synthesis mechanism, structure characterization and modulation, as well as their use as anodes for Li ion batteries were also investigated to provide new insight on the materials chemistry used to produce carbon nanomaterials and their bulk applications for energy storage.

2. Experiment

2.1. Catalyst preparation

The Ni based LDH catalysts were synthesized through the co-precipitation reaction by adding urea into aqueous solution of nickel nitrate and aluminum nitrate similar to our previous reports [23]. $Ni(NO_3)_2{\cdot}6H_2O$, $Al(NO_3)_3{\cdot}9H_2O$ were dissolved in 250 mL deionized water with $[Ni^{2+}] + [Al^{3+}] = 0.15$ mol/L, n(Ni):n(Al) = 3:1. The urea was dissolved in the solution with [urea] = 3.0 mol/L. The as-obtained solution was kept overnight at 100 °C under continuous magnetic stirring (equipped with a reflux condenser in ambient atmosphere) for 9.0 h in a 500.0 mL flask, and then at 94 °C for another 12 h with the stir off. After several steps of filtering, washing, and freeze–drying, the final products of Ni/Al LDH catalyst were available. The other kinds of LDHs were synthesized by similar procedures (Table 1).

2.2. Production of herringbone CNFs in a fixed-bed/fluidized-bed reactor

The herringbone CNFs were synthesized from C_2H_4 over Ni/Al LDH derived catalyst using a CVD method. When a fixed-bed reactor was employed, the reactor with a quartz boat of Ni/Al LDHs was inserted into an electrical furnace at atmosphere pressure. During the synthesis of CNFs, the furnace was heated to 900 °C at a heating rate of 20 °C/min in Ar (100 mL/min), then the LDHs were reduced for 1 h by H_2 (100 mL/min) to nucleate and form the large active Ni particles with well defined crystal surfaces for herringbone CNF deposition. After that, H_2 was stopped and the reduced catalysts were cooled down to the growth temperature to synthesize CNFs in C_2H_4/Ar (100/100 mL/min). Then the reactor was cooled down under Ar atmosphere. The growth temperature was fixed at 500, 550, 600, or 650 °C.

When the fluidized-bed with an inner diameter of 20 mm and a height of 500 mm was employed as the reactor, about 0.5 g Ni/Al LDH catalyst was fed in for CNF deposition. The quartz fluidized bed reactor was heated to 900 °C in H_2/Ar (100/400 mL/min) atmosphere. After 1 h reduction, H_2 was stopped, and the fluidized bed reactor was set to the growth temperature of 550 °C. Ar (500 mL/min) and C_2H_4 (100 mL/min) were introduced into the fluidized bed to start the CNF growth on the Ni/Al LDH flakes. The fluidized bed reactor was cooled down under Ar atmosphere after CNF growth. The as-obtained carbon products were then collected and characterized. To obtain high purity CNFs, the as-obtained samples were treated by NaOH (12.0 mol/L) aqueous solution at 150 °C for 6 h and HCl (5.0 mol/L) aqueous solution at 80 °C for 3 h, subsequently, to remove the LDO flakes. The high purity herringbone CNFs were available after filtering, washing, and freeze–drying. The names of the as-obtained CNF products were defined based on their catalyst composition and growth temperature (as shown in Table 2).

2.3. Characterization

The morphology of the LDH catalysts and the CNF products were characterized by a JSM 7401F scanning electron

Table 1 – A summary of LDH catalyst precursors for CNF synthesis.

LDH catalysts[a]	Anticipated ratio	Experimental ratio[b]	Formula
Ni/Al	3:1	2.7:1	$Ni_{0.73}Al_{0.27}(OH)_2(CO_3)_{0.135}{\cdot}mH_2O$
Ni/Mg/Al	2:1:1	1.4:1:1	$Ni_{0.42}Mg_{0.29}Al_{0.29}(OH)_2(CO_3)_{0.145}{\cdot}mH_2O$
Ni/Cu/Al	2:1:1	1.8:0.9:1	$Ni_{0.49}Cu_{0.24}Al_{0.27}(OH)_2(CO_3)_{0.135}{\cdot}mH_2O$
Ni/Mo/Mg/Al	2:0.2:1:1	1.3:0.08:0.8:1	$Ni_{0.43}Mg_{0.25}Al_{0.32}(OH)_2(CO_3)_{0.133}(MoO_4)_{0.027}{\cdot}mH_2O$

[a] The ratio of the elements is the molar ratio.
[b] The experimental ratio was determined by energy dispersive X-ray spectroscopy (EDX) results.

Table 2 – A summary of CNF products grown on the LDH derived catalysts.

LDH catalyst	Sample ID[a]	Growth temperature (°C)	Surface area (m^2/g)[b]	Purity (%)[c]	DTG-Peak position (°C)[c]
Ni/Al	NA-500	500	148.7	97. 5	441
	NA-550	550	242.4	98.3	454
	NA-550F	550	184.2	97.7	424
	NA-600	600	109.8	97.6	461
	NA-650	650	112.9	/	/
Ni/Mg/Al	NMA-650	650	92.7	96.1	453
Ni/Cu/Al	NCA-600	600	208.4	96.6	428
Ni/Mo/Mg/Al	NMMA-650	650	88.2	93.9	446

[a] The NA-550F CNF sample was obtained in a fluidized-bed reactor, while the other samples were grown in a fixed-bed reactor.
[b] The specific surface area was determined by Brunauer–Emmett–Teller (BET) method.
[c] The results were obtained by Thermo gravimetric (TG) analysis.

microscope (SEM) operated at 3.0 kV and a JEM 2010 high-resolution transmission electron microscope (TEM) operated at 120.0 kV. The EDX analysis was performed using an EDAX apparatus to determine the composition of the as-synthesized LDH catalysts. The level of CNF graphitization as well as the structure of LDHs and the reduced catalysts were determined by X-ray diffraction (XRD) on a Bruker D8 Advance diffractometer at 40.0 kV and 120 mA with Cu K_α radiation. Raman spectra were collected on a Horiba Jobin Yvon LabRAM HR800 Raman spectrophotometer. TG analysis was operated by Mettler Toledo TGA/DSC-1 to collect the data of the purities of CNFs. The N_2 adsorption–desorption isotherms were obtained using an N_2 adsorption analyzer (Autosorb-IQ_2-MP-C system) by N_2 adsorption at 77 K. The specific surface area of all samples was calculated by BET method. The pore size distribution plots were obtained by the non-linear density functional theory method.

2.4. *Li-ion storage performance of herringbone CNFs*

The Li-ion storage performance of herringbone CNFs was evaluated in a two-electrode cell configuration using standard 2025 coin-type cells. A homogeneously slurry was prepared by mixing herringbone CNFs, CNT paste and polyvinylidene difluoride (PVDF) binder in N-methylpyrrolidinone with a mass ratio of CNF:CNT:PVDF = 80:10:10, followed by magnetic stirred for *ca.* 24.0 h. The CNTs were added to improve the electrical conductivity of the anode to illustrate the full potential of Li storage on the CNFs. The slurry was coated onto a Cu foil and dried in a vacuum drying oven at 60 °C for 6.0 h. The as-obtained foil was punched into 13 mm disks as the working electrodes. 1 mm thick Li metal foil was employed as the counter electrode. An electrolyte of $LiPF_6$ (1.0 M) in a mixed solution of ethylene carbonate–dimethyl carbonate–ethylene methyl carbonate with a mass ratio of 1:1:1 was used. A microporous Celgard 2400 membrane was used as the separator. The assembling of cells was conducted in an Ar-filled glove box with oxygen and water content below 1 ppm. The coin cells were monitored in galvanostatic mode within a voltage range of 0.01–3.0 V using Neware multichannel battery cycler. The coulombic efficiency was calculated based on the electrode without conductive CNT paste. The cyclic voltammogram (CV) measurements were performed on a Solartron 1470E electrochemical workstation at a scan rate of 0.1 mV s^{-1}.

3. Results and discussion

3.1. *The Ni based LDH catalysts*

Ni/Al, Ni/Mg/Al, Ni/Cu/Al, as well as Ni/Mo/Mg/Al LDH catalysts were synthesized by a co-precipitation process [23]. Herein, Ni/Al LDH was taken as a model catalyst to illustrate its morphology, structure, and catalytic performance for CNF fabrication. The typical morphology of the as-obtained Ni/Al LDHs is shown in Fig. 1a and b. The Ni/Al LDH flakes were with a thickness of *ca.* 20 nm and a diameter of *ca.* 200 nm. The LDH flakes were agglomerated into a flower-like shape, winding around a core. The "flower" and the "petal" were 500 and 100 nm in size, respectively (Fig. 1a). They were very fluffy and with a low packing density of approximately 200 kg/m^3. The gaps among individual LDH flakes provide free space for catalytic deposition of CNFs.

The typical XRD spectrum of the Ni/Al LDHs was shown in Fig. 1c. The sharp features of the intrinsic diffraction peaks (such as (003), (006), and (009)) suggested that the as-produced LDH flakes afforded a high degree of crystallization. The TG and differential thermogravimetric (DTG)

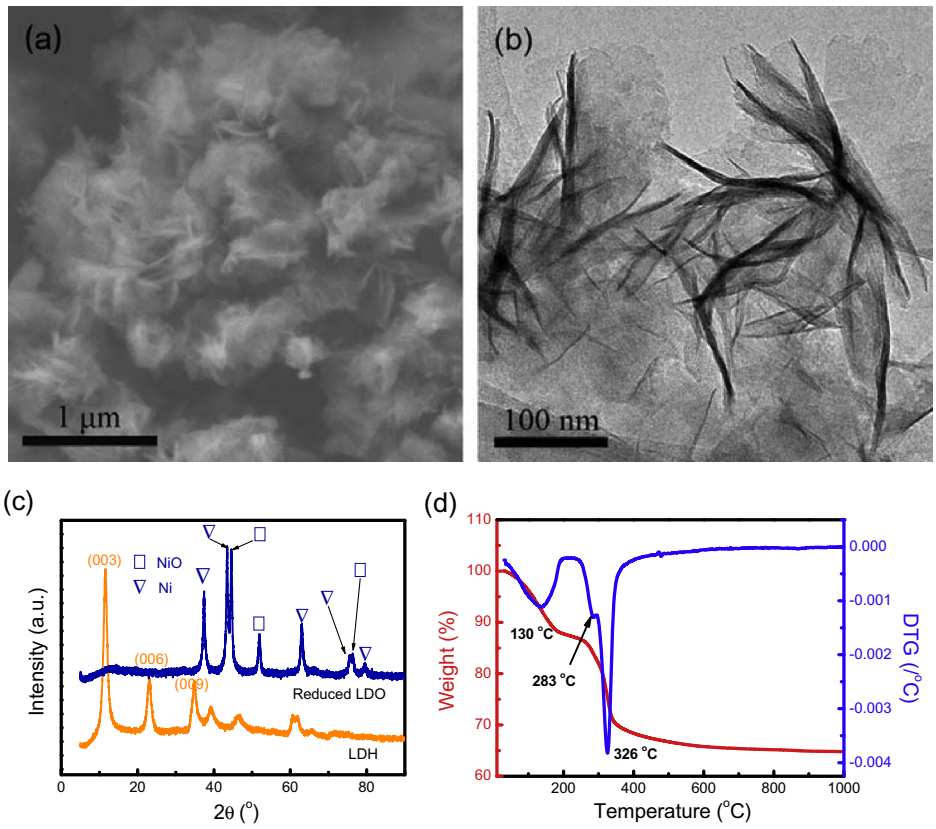

Fig. 1 – The (a) SEM and (b) TEM images of the as-obtained NiAl LDH flakes; (c) XRD patterns of the as-obtained LDHs and reduced catalysts, (d) TG and DTG profiles of the NiAl LDH flakes.

profiles of the Ni/Al LDH catalysts illustrated three weight loss periods at 130, 283, and 326 °C (Fig. 1d). The first weight loss period with a weight loss of 13.3% was attributed to the evaporation of physically adsorbed water from the Ni/Al LDH flakes; the second and third weight loss were mainly attributed to the dehydroxylation and decarbonation of the brucite-like layers, respectively [23,24]. The OH^- and CO_3^{2-} were completely decomposed and oxides are formed after calcination at a temperature over 600 °C.

After the H_2 reduction, embedded Ni NPs were uniformly distributed on the layered double oxide (LDO) support. The flake morphology was partially preserved, while Ni NPs with a size of 20–40 nm and a high density of *ca.* 3×10^{11} cm^{-2} were distributed on the calcined LDO flakes (Fig. 2a and b). Fig. 2c–e illustrated the EDX mapping of selected area in Fig. 2b. The well dispersion of Ni NPs on LDO flakes were detected. There was a significant overlap between Al and O, indicating the Ni were mainly in reduced metal state. The XRD pattern of the reduced catalyst (Fig. 1c) confirmed the reduction of Ni. The weak NiO peaks were available, which was attributed to the oxidation of Ni NPs during the XRD sample preparation and measurement procedure.

3.2. *Herringbone CNFs synthesized from Ni/Al LDH derived catalysts*

With the introduction of carbon source into the fixed-bed reactor at 600 °C, a large amount of CNFs were extended from the agglomerated catalysts. The CNFs were entangled with each other and grown in random directions (Fig. 3a). The average diameter of the as-obtained CNFs was measured as 50 nm (Fig. 3b). There was an approximate 32.9° angle between the orientation of graphitic layers and the *c*-axis of the as-grown CNFs (Fig. 3c and d). The sp^2 domains in the herringbone CNFs were estimated to be with a size of 10–40 nm. Such sp^2 domains were cup-stacked with each other. The edge of graphene nanosheets were directly exposed to the outer wall of the CNFs. Such termination of carbon sheets in herringbone CNFs requires foreign atoms to saturate dangling bonds. Single and multiple loops were formed on the ribbon edges when the samples are annealing at a temperature over 1000 °C [25–27].

A very sharp and strong (002) diffraction peak was detected from the XRD pattern of the as-obtained CNFs (Fig. 4a). The distance between the graphitic layers of the CNFs was around 0.34 nm, which was a bit larger than that of ideal graphite (0.335 nm). Besides, the peaks of Ni NPs were also observed. Fig. 4b showed the Raman spectrum of the CNFs. Both the in-plane vibration of graphitic lattice (G band at 1575 cm^{-1}) and the disorder band aroused from amorphous carbon and edges (D band at 1350 cm^{-1}) were identified. The I_G/I_D of the as-grown NA-600 CNFs was 0.75, indicating the large amount of defects in herringbone CNF products. The ratio was much lower than that of single walled CNTs (>10) [28–30], double walled CNTs (5–12) [31], high quality multi-walled CNTs (1.5–3) [32], and comparable to the value of reduced graphene oxide (rGO) (0.5–1) [33] and other CNFs [34].

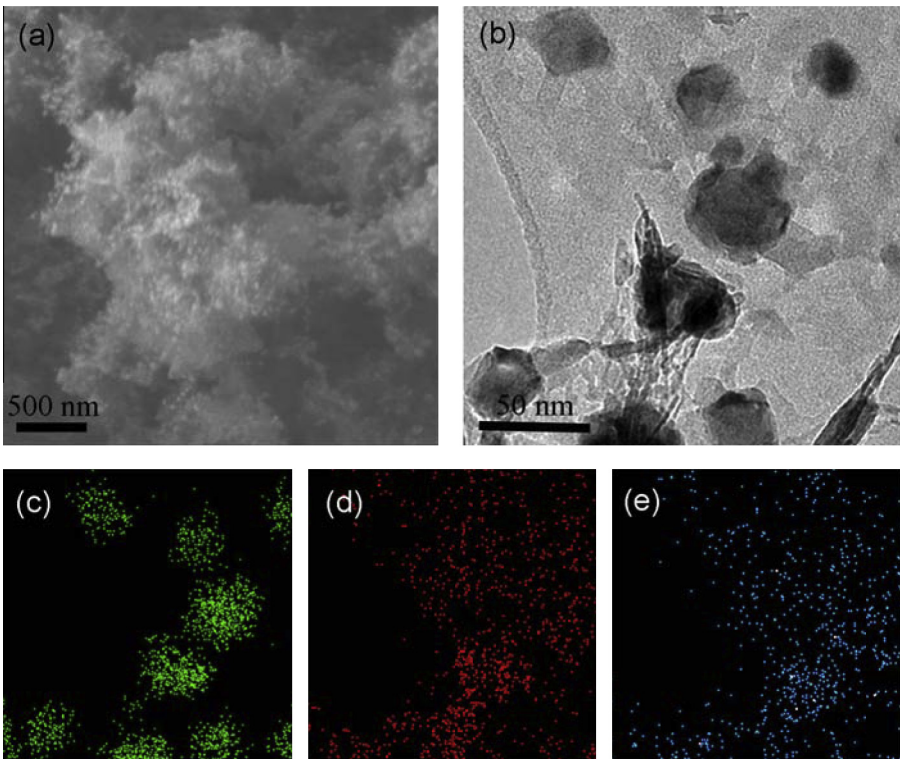

Fig. 2 – The (a) SEM and (b) TEM images of the reduced NiAl catalyst; the (c) Ni, (d) Al, and (e) O element mapping of reduced NiAl LDHs.

A sharp loss of mass to 2.44% was observed in the TG profile of the herringbone CNFs (NA-600) (Fig. 4c) during a temperature window from 450 to 515 °C. The purity of raw CNF was 97.6%, indicating a high carbon yield of *ca.* 40 $g_{CNF}/g_{cat.}$, which was significantly higher than single-walled (~0.001–1 g_{CNT}/g_{cat}) [23], double-walled (~0.01–2 g_{CNT}/g_{cat}) [31], or few-walled CNT (~0.1–30 g_{CNT}/g_{cat}) [34] formation on LDH catalysts. The weight loss peak was placed at around 461 °C, which was lower than that of single- or few-walled CNTs obtained at high growth temperatures [24,31]. This indicates that the carbon atoms in the herringbone CNFs are easily attacked by the oxygen molecules, and the chemisorbed O_2 can be dissociated into mobile atom of oxygen that easily diffuse along the sp^2 carbon planes due to their unique herringbone structure [35,36]. Besides, the herringbone CNFs have a very small sp^2 carbon domain and large spacing between (002) planes. All these facts result in the easy oxidation of the herringbone CNFs at a relatively low temperature.

The N_2 adsorption and desorption isotherms of NA-600 were presented in Fig. 4d. The hysteresis loop was induced by wedge-shaped pores with open ends. A BET specific surface area of 109.8 m^2/g was calculated. The profile of pore size distribution (inserted in Fig. 4d) indicated the fact that both mesopores and micropores are available in the as-obtained CNF products.

3.3. *Robust growth of herringbone CNFs on Ni based catalysts*

The Ni NPs distributed on the LDO flakes efficiently grew herringbone CNFs in the fixed-bed/fluidized-bed reactor at a temperature ranging from 500 to 650 °C. As shown in Fig. 5, herringbone CNFs were robustly grown out. The angles between the orientation of graphitic layers and the *c*-axis of CNFs were mainly distributed from 20° to 60°, which depended on the nanostructure of NPs and related growth parameters. The packing of sp^2 domain was not always regular through the whole fibers. The packing of carbon sheets recorded the unstable interface between sp^2 carbon and NP catalysts. The dissolved carbon atoms in the Ni NPs play a key role in the orientation of sp^2 plane during CVD growth [37], and the concentration of dissolved carbon atoms is not constant when the Ni NPs are catalytically growing CNFs. Such dynamics is well recorded by CNFs, especially the herringbone packing of sp^2 domain in the final products.

The preparation conditions and typical physical properties of as-prepared CNFs were summarized as Table 2. A very high CNF purity of over 97.5% was available on Ni/Al LDH catalyst for every CNF sample. The DTG peaks were ranging from 441 to 461 °C when the herringbone CNFs were grown in the fixed-bed reactor. A highest and lowest BET surface area of 242.4 and 109.8 m^2/g were determined for NA-550 and NA-600, respectively. When the CNFs were grown in a fluidized-bed reactor, the herringbone CNFs were also obtained (Fig. 5c), and a surface area of 184.2 m^2/g on NA-550F was available. The fluidized-bed reactor provides good heat and mass transfer, enough space for CNF volume expansion, as well as continuous feeding of granular catalysts/products [38–42]. Therefore, the fluidized bed is a very promising reactor style to large scale production of herringbone CNFs on LDH catalysts.

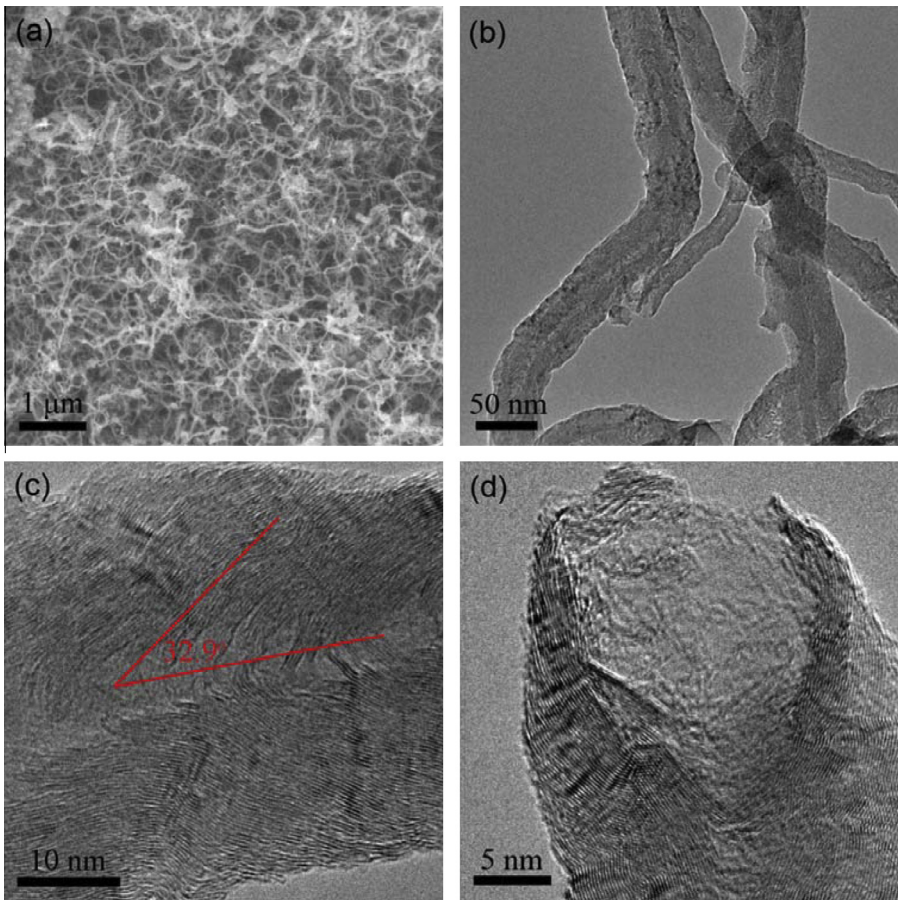

Fig. 3 – The low magnification (a) SEM and (b) TEM images of the NA-600 CNFs synthesized over NiAl LDHs at 600 °C; (c and d) the high magnification TEM images of the NA-600 CNFs.

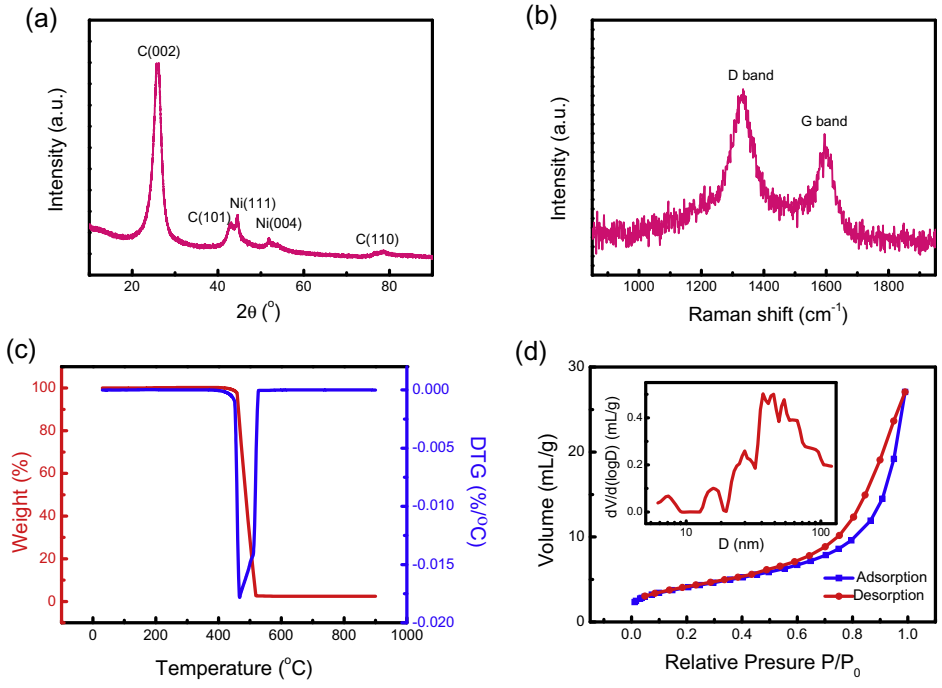

Fig. 4 – (a) The XRD profile, (b) Raman spectrum, (c) TG and DTG curves, and (d) N_2 isothermal adsorption and desorption curves of the NA-600 CNF sample. The inset in (d) is the corresponding pore size distribution of NA-600 CNFs.

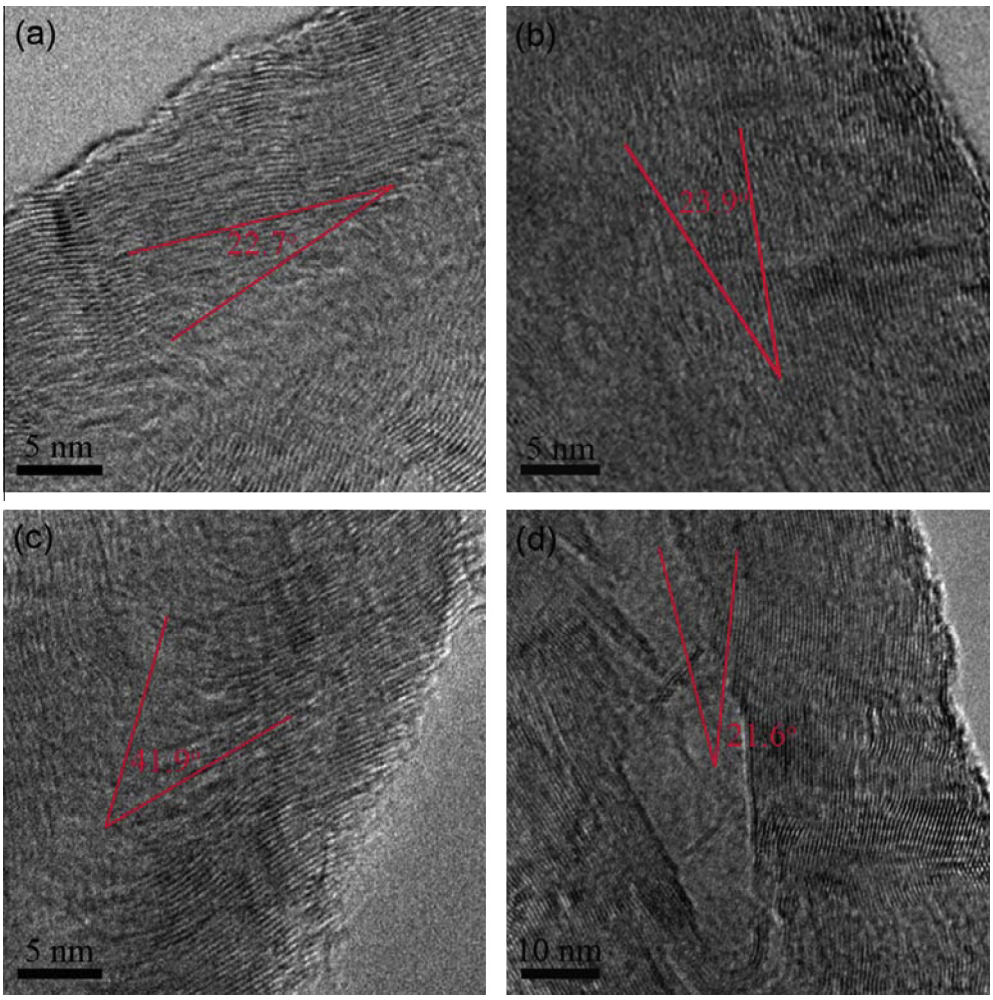

Fig. 5 – The high magnification TEM images of the (a) NA-500, (b) NA-550, (c) NA-550F, and (d) NA-650 herringbone CNFs.

The herringbone CNFs were efficiently produced on other Ni based LDH derived catalysts (Ni/Mg/Al, Ni/Cu/Al, and Ni/Mo/Mg/Al LDHs) (Fig. 6). The hollow cores were detected on the CNFs grown on Ni/Mg/Al or Ni/Mo/Mg/Al catalysts, which was attributed from the weaker metal support interaction between Ni and MgO than that between Ni and Al_2O_3 [43]. The yield and BET surface area of herringbone CNFs were well mediated by the composition of the catalysts rather than the growth temperature and the reactor style. Both the BET specific surface area and purity of the as-obtained CNFs decreased significantly when Ni/Mg/Al and Ni/Mo/Mg/Al LDHs were employed as catalysts (Table 2).

The large Ni NPs with a size of 20–40 nm afford good reactivity for herringbone CNF formation. This is much larger than Ni particles used for single/few-walled CNT formation. The typical interface between the as-grown CNFs and Ni catalyst are shown in Fig. 7. The Ni NP offers a 0.21 nm spacing, which corresponded to (111) planes of Ni catalysts. The deposited CNFs illustrate a 0.34 nm spacing and the sp^2 domain size is very limited. It is more appropriate to use the turbostratic carbon to describe the texture in the nanocarbon products. The angle between the sp^2 carbon domains and Ni catalyst is similar to that reported by Rinaldi et al. [37], indicating the well defined growth direction between the space lattice of CNFs and Ni catalysts. Rather than a catalyst with a liquid state, the large Ni catalyst prefers to be a solid state with certain exposed surface for carbon precipitation. The hydrocarbon feedstock is easy to be decomposed into carbon species. The surface diffusion and lattice directed bulk diffusion of carbon provide the anisotropic precipitation of sp^2 carbon domains. The carbon atoms penetrate into the Ni(111) surface and migrate to octahedral subsurface sites, with an effective energy barrier of 1.92 eV [37]. The Ni NPs also provide a variety of low-coordinate sites for carbon adsorption or absorption, and the coordinate site on different exposed surface is quite different. The deposited carbon can be epitaxially grown on exposed Ni(111) plane and a herringbone structure is available on the embedded Ni catalysts. The Ni catalysts can be well mediated by a polymer protector [44] or promoter pinning [17] to inhibit their aggregation. Therefore, the CNF morphologies are expected to be well mediated by the combination of catalyst design and growth procedures.

3.4. *Li ion storage performance of herringbone CNFs*

The herringbone CNFs are promising candidates for anode materials in Li-ion batteries. The electrochemical performances of herringbone CNFs were evaluated with 2025-type

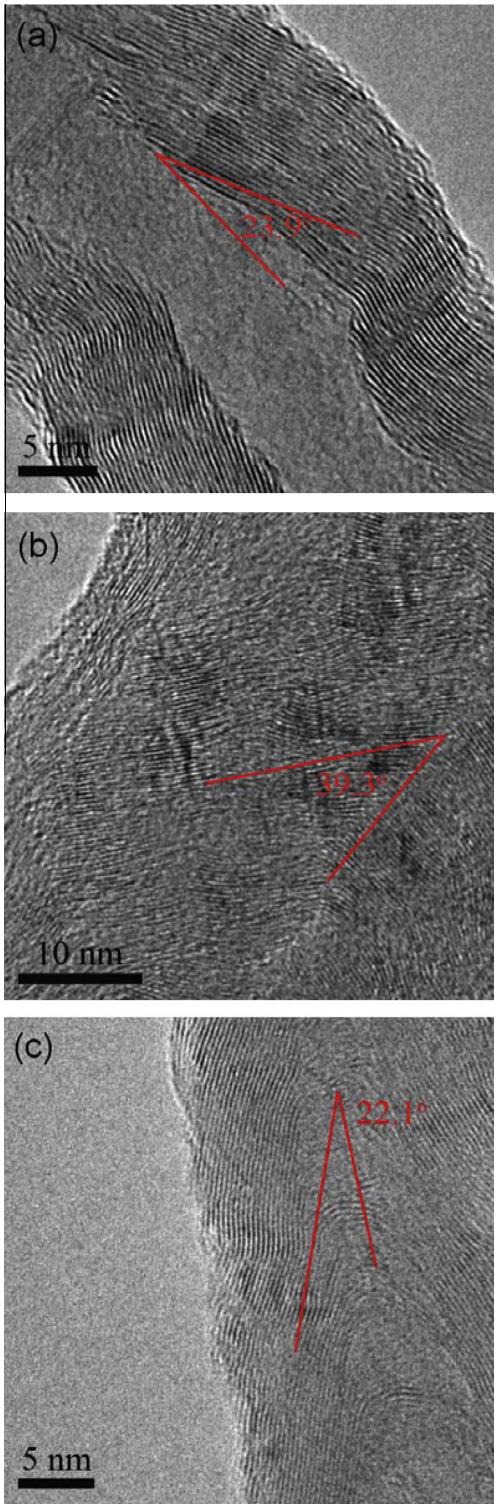

Fig. 6 – The high magnification TEM images of the (a) NMA-650, (b) NCA-600, and (c) NMMA-650 herringbone CNFs.

coin half-cells. The CV profiles of NA-550 CNFs with the operation voltage in the range of 0.01 to 3.0 V *vs.* Li/Li^+ was shown in Fig. 8a. There were two cathodic peaks in the first cycles. The first one was a prominent cathodic peak at 0.58 V *vs.* Li/Li^+ in the first cycle, which disappeared in the following cycles. Such cathodic peak corresponded to the irreversible reactions, such as the reactions between solvent Li^+ with oxygenic groups on the CNF surface and solvent degradation, which resulted in the formation of solid electrolyte interface (SEI). The second cathodic peak at 0.05 V *vs.* Li/Li^+ corresponded to the insertion of Li^+ into the graphitic structure. In the anodic scan, the Li^+ was extracted from the herringbone CNFs at *ca.* 0.1 V *vs.* Li/Li^+. After the potential is swept past 0.5 V, the anodic current decreased due to the depletion of lithium ions from the CNFs and the anodic current fell to smaller values as the potential approaching 3.0 V [12]. After an activation process by the first redox, the Li^+ insertion/extraction peaks of the following cycles became sharper and more intense. The curves of the subsequent three cycles were in good superposition, indicating high reversibility of herringbone CNF anodes in Li-ion storage.

The galvanostatic charge-discharge profiles of herringbone CNF and CNT anodes were shown as Fig. 8b. The NA-550 CNF anode exhibited a typical cycle discharge and charge capacity of 374 and 330 mAh g^{-1}, respectively which were higher than high-surface-area nanocarbon materials (*e.g.* graphene, few-walled CNTs [13,45,46]). The irreversible capacity of nanocarbon materials was mainly caused by the formation of SEI. Furthermore, the shape of the discharge and charge curves was similar to those observed previously from CNT and/or graphene anode [13,45,46]. Such extraordinary Li storage performance with quite high coulombic efficiency is attributed to the excellent electronic conductivity, short sp^2 carbon domain, and low surface area of the herringbone CNFs.

The rate performance of the NA-550 anode was shown as Fig. 8c. The NA-550 exhibited a reversible discharge capacity of 374 or 119 mAh g^{-1} at a charge–discharge current of 0.2 or 5.0 °C, respectively. The rate performance of the herringbone CNFs was similar to that of CNTs. The cycling performance of CNFs at 0.5 °C was also evaluated (Fig. 8d). The initial, 10th, and 100th discharge capacity of NA-550 were 332, 267, and 235 mAh g^{-1}, respectively. After the rapid capacity decay during the initial 10 cycle, a stable cycling performance was observed for the herringbone CNF sample. The discharge capacity of NA-600 was low and a similar trend in degradation was detected.

A CNT sample mass produced by fluidized bed CVD on Fe based catalysts was also included. The CNTs afforded an higher discharge capacity of 449 mAh g^{-1}. The discharge capacity and coulombic efficiency at 0.2 °C were correlated with the specific surface area as indicated in the Fig. 9. With the increase of the surface area of nanocarbon, the discharge capacity rise at a rate of 0.90 mAh cm^{-2}. During the discharge process, the Li ions intercalate into the graphene layers of CNFs. When the surface area is high, the size of sp^2 carbon layer is small for CNF samples. Consequently, a large amount of graphene edges is provided for Li ions intercalated into the CNF materials, leading to a higher discharge capacity at a given current density. The coulombic efficiency illustrated an opponent trend: the initial coulombic efficiency was 0.540 and 0.452 for NA600 and NA550 with a surface area of 109.8 and 242.4 m^2/g, respectively. It increased to 0.887 and 0.828 for NA600 and NA550, respectively, during the second cycle. The SEI layer attached on the outer layer of CNFs consumes more Li ions, leading to a low initial coulombic efficiency at the first cycle. If the initial coulombic efficiency

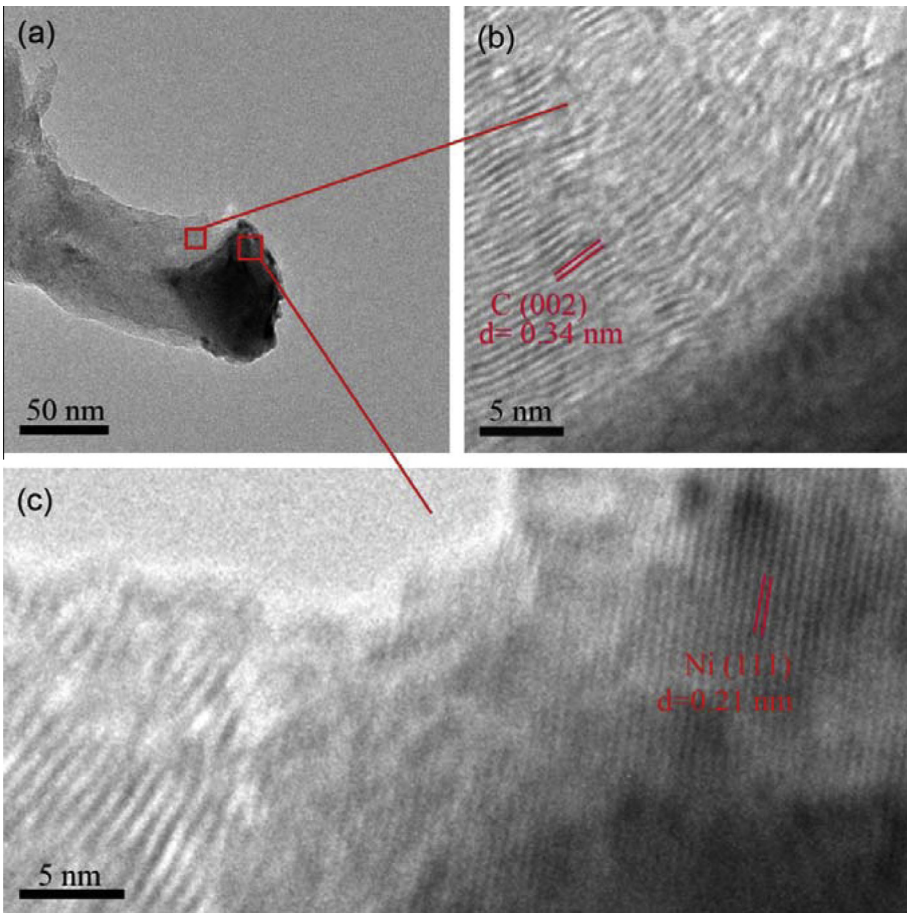

Fig. 7 – (a) The low and (b and c) high magnification TEM images of the NA-600 CNFs with the Ni catalysts attached at the tip of the nanofibers.

becomes higher, the amount of Li ions consumed in the formation of SEI layers can be reduced, which favored the overall energy density of batteries. Low surface area of CNFs affords high initial coulombic efficiency and large diameter. Similar to vapor grown carbon fibers, the herringbone CNFs are also anticipated to be extraordinary additive into graphite powder or mesophase microbead anode for high performance Li-ion battery for the following reasons: (1) The herringbone CNFs interconnect between the granular anode to form a 3D continuous conductive network, which improves the conductivity of the anode; (2) the 1D CNFs render the ability to absorb and retain significant electrolyte and provide resiliency and compressibility to the electrode structure, which guarantees good conductive network during the reversible charge-discharge process [47,48]; (3) the CNFs also afford acceptable Li ion storage performance. More experimental investigation to demonstrate the potential of herringbone CNFs as anode additive is highly expected.

4. Conclusion

The Ni based LDHs were employed as efficient and effective catalyst precursors for robust growth of herringbone CNFs by catalytic CVD. The herringbone CNFs were available in high purity (>97.4%) on $Ni_{0.73}Al_{0.27}(OH)_2(CO_3)_{0.135}{\cdot}mH_2O$ LDH catalyst. The Ni NPs with a size of 20–40 nm and a high density of *ca.* 3×10^{11} cm^{-2} were distributed on the calcined LDO flakes when the LDH was reduced at 900 °C for 1 h. They were effective metal catalysts for CNF deposition. When the CNFs were grown at 600 °C on Ni/Al catalyst, the as-obtained products have an outer diameter of *ca.* 50 nm, a specific surface area of 109.8 m^2 g^{-1}, an I_G/I_D ratio of 0.75, and a weight loss peak at around 461 °C. The Ni particles distributed on the Ni/Al LDO flakes robustly grew herringbone CNFs at a temperature ranging from 500 to 650 °C. The Ni/Mg/Al, Ni/Cu/Al, and Ni/Mo/Mg/Al LDHs were also efficient catalysts for herringbone CNF growth. When the herringbone CNFs grown at 550 °C were served as anodes for Li ion battery applications, a reversible capacity of 330 mAh g^{-1} and initial coulombic efficiency of 45.2% was demonstrated. With the specific surface area increasing, the discharge capacity increased at a rate of 0.90 mAh cm^{-2}, while the initial coulombic efficiency decreased gradually on nanocarbon anodes. The as-obtained CNFs afford a high discharge capacity, which is a promising additive for the anodes in the Li ion cells.

Acknowledgments

The authors thank Hongjie Peng and Xinyan Liu for helpful discussion. This work was supported by National Basic Research Program of China (973 Program, 2011CB932602).

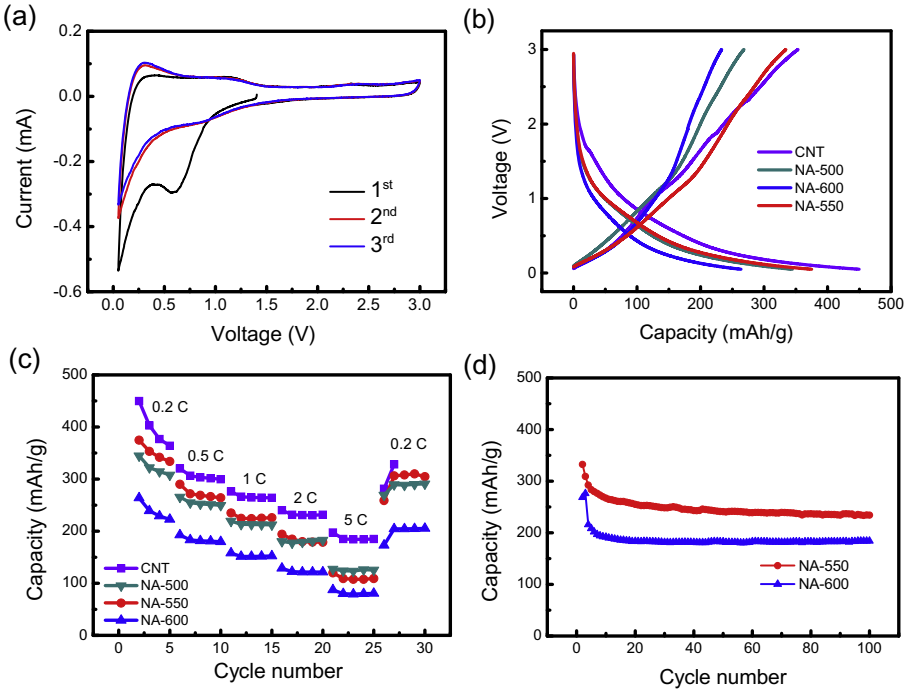

Fig. 8 – The Li-ion storage performance on herringbone CNFs: (a) the CV profiles of NA-550; (b) the voltage profiles of the initial galvanostatic charge-discharge on herringbone CNF and CNT anodes at a current rate of 0.2 °C; (c) the discharge capacities of CNF and CNT anodes at different current densities; (d) the cycling performance of CNF anodes at 0.5 °C.

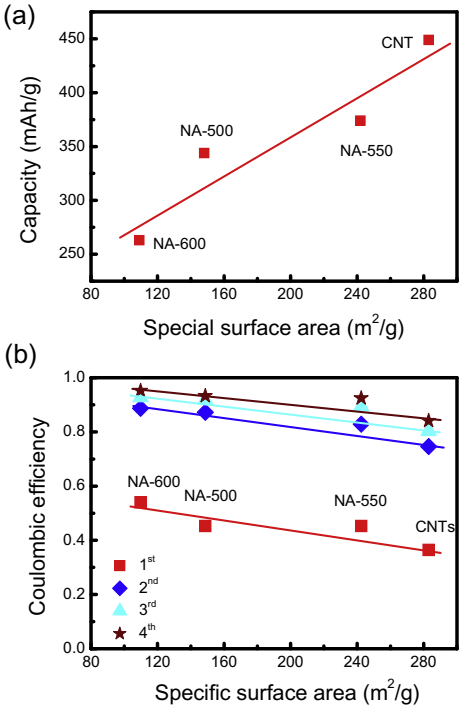

Fig. 9 – (a) The relationship between the surface area *vs.* the discharge capacity of nanocarbon at a current rate of 0.2 °C; (b) the relationship between coulombic efficiency at a current rate of 0.2 °C *vs.* the specific surface area. The coulombic efficiency refers to the ratio of the take-off and build-in lithium capacity in one cycle.

REFERENCES

[1] Liu ZF, Jiao LY, Yao YG, Xian XJ, Zhang J. Aligned, ultralong single-walled carbon nanotubes: from synthesis, sorting, to electronic devices. Adv Mater 2010;22(21):2285–310.

[2] Jiang KL, Wang JP, Li QQ, Liu L, Liu CH, Fan SS. Superaligned carbon nanotube arrays, films, and yarns: a road to applications. Adv Mater 2011;23(9):1154–61.

[3] Zheng RT, Zhao Y, Liu HP, Liang CL, Cheng GA. Preparation, characterization and growth mechanism of platelet carbon nanofibers. Carbon 2006;44(4):742–6.

[4] Zhao TJ, Kvande I, Yu YD, Ronning M, Holmen A, Chen D. Synthesis of platelet carbon nanofiber/carbon felt composite on *in situ* generated Ni–Cu nanoparticles. J Phys Chem C 2011;115(4):1123–33.

[5] Duan XZ, Qian G, Zhou JH, Zhou XG, Chen D, Yuan WK. Flat interface mediated synthesis of platelet carbon nanofibers on Fe nanoparticles. Catal Today 2012;186(1):48–53.

[6] Kim YA, Hayashi T, Naokawa S, Yanaisawa T, Endo M. Comparative study of herringbone and stacked-cup carbon nanofibers. Carbon 2005;43(14):3005–8.

[7] Jiang JJ, Tang XL, Wu R, Lin HQ, Qu MZ. Electrochemical performance of polygonized carbon nanofibers as anode materials for lithium-ion batteries. Particuology 2013;11(4):401–8.

[8] Ji J, Duan XZ, Qian G, Zhou XG, Chen D, Yuan WK. *In situ* production of Ni catalysts at the tips of carbon nanofibers and application in catalytic ammonia decomposition. Ind Eng Chem Res 2013;52(5):1854–8.

[9] Fu XB, Yu H, Peng F, Wang HJ, Qian Y. Facile preparation of RuO_2/CNT catalyst by a homogenous oxidation precipitation method and its catalytic performance. Appl Catal A 2007;321(2):190–7.

[10] Zhang Q, Huang J-Q, Zhao M-Q, Qian W-Z, Wei F. Carbon nanotube mass production: principles and processes. ChemSusChem 2011;4(7):864–89.
[11] Zhang Q, Huang JQ, Qian WZ, Zhang YY, Wei F. The road for nanomaterials industry: a review on carbon nanotube production, post-treatment, and bulk applications for composite and energy storage. Small 2013;9(8):1237–65.
[12] Lee BS, Son SB, Park KM, Yu WR, Oh KH, Lee SH. Anodic properties of hollow carbon nanofibers for Li-ion battery. J Power Sources 2012;199:53–60.
[13] Fan ZJ, Yan J, Wei T, Ning GQ, Zhi LJ, Liu JC, et al. Nanographene-constructed carbon nanofibers grown on graphene sheets by chemical vapor deposition: high-performance anode materials for lithium ion batteries. ACS Nano 2011;5(4):2787–94.
[14] Zhu J, Holmen A, Chen D. Carbon nanomaterials in catalysis: proton affinity, chemical and electronic properties, and their catalytic consequences. ChemCatChem 2013;5(2):378–401.
[15] Zhao MQ, Zhang Q, Huang JQ, Wei F. Hierarchical nanocomposites derived from nanocarbons and layered double hydroxides – properties, synthesis, and applications. Adv Funct Mater 2012;22(4):675–94.
[16] Xu ZP, Zhang J, Adebajo MO, Zhang H, Zhou CH. Catalytic applications of layered double hydroxides and derivatives. Appl Clay Sci 2011;53(2):139–50.
[17] Zhao MQ, Zhang Q, Zhang W, Huang JQ, Zhang YH, Su DS, et al. Embedded high density metal nanoparticles with extraordinary thermal stability derived from guest–host mediated layered double hydroxides. J Am Chem Soc 2010;132(43):14739–41.
[18] An Z, He J, Duan X. Catalysts with catalytic sites highly dispersed from layered double hydroxide as precursors. Chin J Catal 2013;34(1):225–34.
[19] Zhao MQ, Zhang Q, Jia XL, Huang JQ, Zhang YH, Wei F. Hierarchical composites of single/double-walled carbon nanotubes interlinked flakes from direct carbon deposition on layered double hydroxides. Adv Funct Mater 2010;20(4):677–85.
[20] Sun J, Liu HM, Chen X, Evans DG, Yang WS, Duan X. Carbon nanorings and their enhanced lithium storage properties. Adv Mater 2013;25(8):1125–30.
[21] Li YD, Chen JL, Chang L. Catalytic growth of carbon fibers from methane on a nickel–alumina composite catalyst prepared from Feitknecht compound precursor. Appl Catal A 1997;163(1–2):45–57.
[22] Zhang L, Zhang CF, Xiang X, Li F. Synthesis of novel submicrometer-scale flat carbon fibers and application in the electrooxidation of methanol. Chem Eng Technol 2010;33(1):44–51.
[23] Zhao MQ, Zhang Q, Huang JQ, Nie JQ, Wei F. Layered double hydroxides as catalysts for the efficient growth of high quality single-walled carbon nanotubes in a fluidized bed reactor. Carbon 2010;48(11):3260–70.
[24] Tian GL, Zhao MQ, Zhang Q, Huang JQ, Wei F. Self-organization of nitrogen-doped carbon nanotubes into double-helix structures. Carbon 2012;50(14):5323–30.
[25] Endo M, Kim YA, Hayashi T, Yanagisawa T, Muramatsu H, Ezaka M, et al. Microstructural changes induced in "stacked cup" carbon nanofibers by heat treatment. Carbon 2003;41(10):1941–7.
[26] Gan L, Du HD, Li BH, Kang FY. Enhanced oxygen reduction performance of pt catalysts by nano-loops formed on the surface of carbon nanofiber support. Carbon 2008;46(15):2140–3.
[27] Zhou JH, Sui ZJ, Li P, Chen D, Dal YC, Yuan WK. Structural characterization of carbon nanofibers formed from different carbon-containing gases. Carbon 2006;44(15):3255–62.
[28] Zhao MQ, Zhang Q, Tian GL, Huang JQ, Wei F. Space confinement and rotation stress induced self-organization of double-helix nanostructure: a nanotube twist with a moving catalyst head. ACS Nano 2012;6(5):4520–9.
[29] Yu B, Liu C, Hou PX, Tian Y, Li SS, Liu BL, et al. Bulk synthesis of large diameter semiconducting single-walled carbon nanotubes by oxygen-assisted floating catalyst chemical vapor deposition. J Am Chem Soc 2011;133(14):5232–5.
[30] Zhao MQ, Huang JQ, Zhang Q, Nie JQ, Wei F. Stretchable single-walled carbon nanotube double helices derived from molybdenum-containing layered double hydroxides. Carbon 2011;49(6):2148–52.
[31] Zhang Q, Qian WZ, Wen Q, Liu Y, Wang DH, Wei F. The effect of phase separation in Fe/Mg/Al/O catalysts on the synthesis of DWCNTs from methane. Carbon 2007;45(8):1645–50.
[32] Zhang Q, Huang JQ, Zhao MQ, Qian WZ, Wang Y, Wei F. Radial growth of vertically aligned carbon nanotube arrays from ethylene on ceramic spheres. Carbon 2008;46(8):1152–8.
[33] Chen CM, Huang JQ, Zhang Q, Gong WZ, Yang QH, Wang MZ, et al. Annealing a graphene oxide film to produce a free standing high conductive graphene film. Carbon 2012;50(2):659–67.
[34] Zhang L, Li F, Xiang X, Wei M, Evans DG. Ni-based supported catalysts from layered double hydroxides: tunable microstructure and controlled property for the synthesis of carbon nanotubes. Chem Eng J 2009;155(1–2):474–82.
[35] Marsh H, Rodriguez-Reinoso F. Activated carbon. Amsterdam: Elsevier; 2006. p. 243–321.
[36] Zhao MQ, Zhang Q, Huang JQ, Tian GL, Chen TC, Qian WZ, et al. Towards high purity graphene/single-walled carbon nanotube hybrids with improved electrochemical capacitive performance. Carbon 2013;54:403–11.
[37] Rinaldi A, Tessonnier JP, Schuster ME, Blume R, Girgsdies F, Zhang Q, et al. Dissolved carbon controls the initial stages of nanocarbon growth. Angew Chem Int Ed 2011;50(14):3313–7.
[38] Philippe R, Moranqais A, Corrias M, Caussat B, Kihn Y, Kalck P, et al. Catalytic production of carbon nanotubes by fluidized-bed CVD. Chem Vapor Depos 2007;13(9):447–57.
[39] See CH, Harris AT. A review of carbon nanotube synthesis *via* fluidized-bed chemical vapor deposition. Ind Eng Chem Res 2007;46(4):997–1012.
[40] Danafar F, Fakhru'l-Razi A, Salleh MAM, Biak DRA. Fluidized bed catalytic chemical vapor deposition synthesis of carbon nanotubes – a review. Chem Eng J 2009;155(1–2):37–48.
[41] Zhang Q, Zhao MQ, Huang JQ, Liu Y, Wang Y, Qian WZ, et al. Vertically aligned carbon nanotube arrays grown on a lamellar catalyst by fluidized bed catalytic chemical vapor deposition. Carbon 2009;47(11):2600–10.
[42] Zhang Q, Zhao MQ, Huang JQ, Nie JQ, Wei F. Mass production of aligned carbon nanotube arrays by fluidized bed catalytic chemical vapor deposition. Carbon 2010;48(4):1196–209.
[43] Chen JL, Qiao YH, Li YD. Modification of ni state to promote the stability of Ni–Al_2O_3 catalyst in methane decomposition to produce hydrogen and carbon nanofibers. J Solid State Chem 2012;191:107–13.
[44] Li P, Zhao Q, Zhou XG, Yuan WK, Chen D. Enhanced distribution and anchorage of carbon nanofibers grown on structured carbon microfibers. J Phys Chem C 2009;113(4):1301–7.
[45] Landi BJ, Ganter MJ, Cress CD, Di Leo RA, Raffaelle RP. Carbon nanotubes for lithium ion batteries. Energy Environ Sci 2009;2(6):638–54.

[46] Liu XM, Huang ZD, Oh SW, Zhang B, Ma PC, Yuen MMF, et al. Carbon nanotube (CNT)-based composites as electrode material for rechargeable Li-ion batteries: a review. Compos Sci Technol 2012;72(2):121–44.
[47] Endo M, Kim C, Nishimura K, Fujino T, Miyashita K. Recent development of carbon materials for Li ion batteries. Carbon 2000;38(2):183–97.
[48] Endo M, Kim YA, Hayashi T, Nishimura K, Matusita T, Miyashita K, et al. Vapor-grown carbon fibers (VGCFs) – basic properties and their battery applications. Carbon 2001;39(9):1287–97.